Flow, suspension and mixing dynamics in DASGIP bioreactors, Part 2

Jasmin J. Samaras[1] | Andrea Ducci[2] | Martina Micheletti[1]

[1]Advanced Centre for Biochemical Engineering, University College London, London, UK

[2]Department of Mechanical Engineering, University College London, London, UK

Correspondence
Martina Micheletti, Advanced Centre for Biochemical Engineering, University College London, Bernard Katz Building, Gower Street, London WC1E 6BT, UK.
Email: m.micheletti@ucl.ac.uk

Abstract

This work aims to characterize the mixing and suspension dynamics occurring within two commercially available DASGIP bioreactor configurations, equipped with a two-blade paddle impeller with large impeller to tank diameter ratio, $D/T = 0.97$. Both continuous and intermittent agitation modes were employed to determine the impact that agitation strategy has upon mass transfer and microcarrier settling/suspension. This paper builds upon the flow dynamics data presented in Part 1 for a flat bottom DASGIP bioreactor and shows how intermittent agitation can break-up regions of slow mixing observed during continuous agitation, therefore substantially increasing the mixing efficiency of the system. Similarly, it was found that microcarrier characteristics might significantly affect the level of suspension when the impeller is in dwell status when intermittent agitation modes are used.

KEYWORDS
agitation modes, DASGIP, microcarriers, mixing dynamics, suspension dynamics

1 | INTRODUCTION

Reproducible and scalable cell culture protocols are necessary to further develop and commercialize cell-based therapeutics. In contrast to traditional monolayer-based cultures, three-dimensional (3D) cell culture techniques offer an attractive platform to increase productivity and improve monitoring and control. In this case however, mixing and suspension dynamics play a crucial role, and bioreactor operating conditions must be carefully selected to provide an optimal environment for cell growth. Cells cultured within a heterogeneous system, due to either poor suspension and/or mixing, are exposed to spatial gradients in oxygen, pH, nutrients and temperature. This is especially true for large scale operation, resulting in compromised cell viability, proliferation, differentiation pathways, metabolism and achievable overall yields.[1] The first section of this introduction focuses on suspension dynamics, with direct implications on 3D culture techniques (i.e., embryoid bodies [EB] or microcarrier [MC]-based), while the second section addresses mixing characteristics in commercial bioreactors.

Suspension performances within a reactor are commonly determined using the Zwietering criterion, which consists in finding the minimum rotational speed corresponding to particles at rest for less than 2 s on the base of a reactor.[2] The "just suspended speed," N_{js}, can be calculated from Equation (1):

$$N_{js} = \frac{S D_p^{0.2} \left(\frac{g \Delta \rho}{\rho_L}\right)^{0.45} \upsilon^{0.1} X^{0.13}}{D^{0.85}} \quad (1)^3$$

where S is a dimensionless parameter, depending on the impeller clearance, C, and impeller diameter, D, particle diameter, D_p, fluid–solid density difference, $\Delta \rho$, liquid density, ρ_L, fluid kinematic viscosity, υ, and solids percentage, X. This correlation was originally developed for chemical engineering applications, such as suspension of catalysts and reaction products and batch-wise dissolution of solids, with solid particle densities nearly three-times greater than those of MCs or EB in typical bioprocesses. As a consequence,

Equation (1) was found to over predict N_{js} of MCs by nearly 50%.[4] MCs are in fact highly porous and their effective solid density should be estimated from Equation (2) before using the N_{js} correlation in Equation (1).

$$\rho_{s,eff} = (1-\Phi)\rho_s + \Phi\rho_L \qquad (2)^5$$

When adherent-dependent cells, such as stem cells, are cultured within a 3D bioreactor, they are typically grown in the form of EB, that is, adhered to one another, or on the surface of MC. Both the degree of suspension and settling will depend upon the bioreactor and impeller configuration, the operating conditions employed, as well as EB/MC size, morphology and density. In fact, these three properties are likely to change over the course of a cell culture. For example, EB aggregates of iPSCs were found to increase in size 25% over the course of differentiation to cardiomyocytes,[6,7] while cell elongation of iPSC EBs was achieved during differentiation to neuronal cells with further morphological changes noted as the cells matured.[8] Similarly, commercially available MCs, such as Cytodex, Cytopore (both GE Healthcare), Hillex, (SoloHill) and Cultispher (Percell Biolytica) vary significantly in shape, size, density, material, surface charge or coating and may be microporous or macroporous in structure.[9] Seldom studies have been undertaken investigating how different MC types affect cell culture. Rafiq et al[10] systematically investigated culture of hBMSCs on 13 MC types and found that Plastic SoloHill MCs were the most favorable in terms of growth kinetics, amenability to xeno-free processing and ease of cell harvest from the MC surface. This study highlighted the influence that MC selection may have upon biological outcomes but lacked a comparison from an engineering perspective. Nienow et al[11] provided an engineering characterization with direct link to the cell culture process. They first investigated the suspension dynamics of plastic SoloHill MCs in a flat-bottom DASGIP bioreactor equipped with a pitched blade impeller and then performed an hBMSC proliferation culture at the just suspended speed identified. In this work cells were successfully cultured at N_{js}, for cell culture densities of $1-5 \times 10^5$ cells/ml, however it was indicated that the just suspended speed may not provide sufficient oxygen mass transfer for higher cell densities. An extensive comparison was also made between the Kolmogorov length scale, λ, based on the mean energy dissipation rate and the MC size. They found that for their DASGIP cell culture λ was 30% the MC diameter. Similar analysis was carried out by Collignon et al,[12] who compared the shear stress levels and Kolmogorov length scales of different types of axial impellers when working at MC just suspended speed, N_{js}. The ratio between the Kolmogorov length scale and MC diameter was $\lambda/D_p = 0.51-0.89$ for the different impeller types. The study showed that the TTP impeller (Mixel) and the Elephant Ear impeller (Applikon) produced the smallest mechanical constraints at their just-suspended speed and were the most advantageous even at speeds greater than N_{js}.

Most engineering studies address flow, suspension and mixing dynamics for continuous agitation conditions, however it must be noted that intermittent agitation modes are often used in cell attachment protocols on MCs[11,13,14] and in differentiation procedures.[6,7,15]

From this point of view it is also worth to mention the work of Steiros et al[16] who carried out torque and power measurements for transient conditions, step change and quasi stationary regimes.

Quantification and assessment of mixing dynamics in 3D cell cultures is crucial towards process optimization and avoidance of culture heterogeneities.[17] Ozturk[18] observed cell lysis from locally elevated pH levels within the region of base addition in a mammalian cell culture. Similarly, Langheinrich and Nienow[19] observed significant differences in pH (up to 1.0 unit), between the bulk flow region and the point of base insertion, to levels potentially detrimental to cell viability. They concluded that assessment of spatial and temporal mixing dynamics could aid in selecting the location of base addition or in determining the best operating conditions to prevent large pH variations. The work of Ducci and Yianneskis[20] directly investigated the impact of feed location upon mixing. They showed a 20–30% reduction in measured mixing times when feed insertion was made in the vortex core of precessional macroinstabilities, while further enhancement was predicted by the experimental data of Doulgerakis et al[21] in proximity of the impeller blades due to the combined action of impeller trailing vortices and macroinstability structures.

Most mixing dynamics characterization in the literature typically refer to standard stirred tank geometries, seldom mixing characterization has been considered for commercial bioreactors, equipped with non-standard impeller geometries such as the large impeller D/T used in this work, and to the author's knowledge there are no works in the literature which address mixing performance under intermittent agitation modes.

Flow regime is very important for EB or MC-cell culture with regards to cell attachment, viability, growth and differentiation yields. A balance is sought such as to achieve full suspension and efficient mixing, ensuring spatial and temporal homogeneity, with optimal shear stresses and turbulence imparted to avoid loss of cell viability, cell detachment or undesirable differentiation pathways. The present study stems from the work of Correia et al[6] and Samaras et al[7] who have shown that intermittent agitation strategies are beneficial for differentiation yields of iPSCs to cardiomyocytes and builds upon the flow dynamics investigation in Part 1 to provide an in-depth assessment of suspension and mixing for commercial bioreactors equipped with a large impeller D/T operated under both continuous and intermittent modes of agitation.

2 | MATERIALS AND METHODS

2.1 | Bioreactor configuration

A flat- and round-bottomed DASGIP Cellferm-pro bioreactor system (Eppendorf, Germany), with heights, $H = 15.5$ and 16.5 cm and internal diameter, $T = 6.2$ cm, were equipped with a 6 cm diameter trapezoidal paddle impeller at an off-bottom clearance, $C = 1$ cm ($D/T = 0.97$, $C/H_L = 0.15$) and $C = 1.95$ cm ($D/T = 0.97$, $C/H_L = 0.26$), respectively. A schematic of each bioreactor configuration is given in Part 1, Figure 1a. A working volume of $V_w = 0.20$ L was used in both

configurations, corresponding to liquid heights, H_L = 6.62 and 7.4 cm for the flat and round bottom bioreactor, respectively. To fully customize the agitation programme the impeller shaft was extended and attached to an N-Series Allen Bradley Motor unit. To minimize optical distortion due to the curvature of the vessel the system was mounted within a water filled glass trough shown in Figure 1.

2.2 | Suspension characterization experiments

Suspension characterization measurements were performed using the experimental set up of Figure 1, with a mounted high-speed NET iCube camera (NET, Germany) connected to an adjustable arm. A white LED panel was installed behind the reactor to obtain a uniform background.

Reference conditions for continuous agitation were obtained for N = 10–200 rpm to investigate the minimum speed, N_H, required to achieve MC homogeneity within the tank volume. Intermittent agitation modes with impeller start and stop were also investigated and three-time components were defined: (a) the impeller revolution time, $T = 1/N$; (b) the interval time, T_{inv}, during which the impeller is in motion; and (c) the dwell/stop time, T_{dwell}, during which the impeller is idle. Intermittent agitation modes were investigated for a fixed impeller rotational speed and interval time, N = 90 rpm, T_{inv} = 30 s, while the dwell time was varied in the range, T_{dwell} = 500–30,000 ms.

Three commercially available MCs were used for suspension characterization: Cytopore 1, Cytodex 3 and Cultispher-G (see Table 1). They were selected to mimic EB properties at different time points during cell culture, as described in References 6 and 7 These works report a 25% increase in EB size over the course of cardiogenic differentiation, in addition to a 45% increase in EB settling. This was taken into account using MCs with similar density ($\rho \approx 1.04$ g/cm^3), but with varying combination of size and porosity, which results in different effective density (Table 1). Microscope images of each MC type are also provided for illustration at ×120 and ×600 magnification using an inverted brightfield microscope.

Similar to the work of Olmos et al, MCs were stained using 0.4% Trypan Blue (Sigma-Aldrich, United States),[22] and all experiments were conducted at a fixed concentration of 1 g/L. Images for each condition were then recorded at a frequency of 2 Hz for 5 min for all agitation modes. The MCs were then allowed to fully settle in-between experiments and images were processed using a purposely-written MATLAB code.

As images were recorded from the side of the vessel, a direct measurement of MC homogeneity across the reactor volume was obtained. In the following, a fully homogeneous distribution of MCs corresponds to a fully suspended environment. The suspension/homogeneity index, $H(N)$, was determined from Equation (3):

$$H(N) = \frac{(I_0 - I_N)}{(I_0 - I_{max})} \tag{3}$$

where I_N is the cumulative brightness of the image at speed N, I_0 represents the image brightness when the system is stationary and fully settled and I_{max} denotes when the system is completely suspended and homogeneous. The data were fitted with the sigmoidal function of Equation (4):
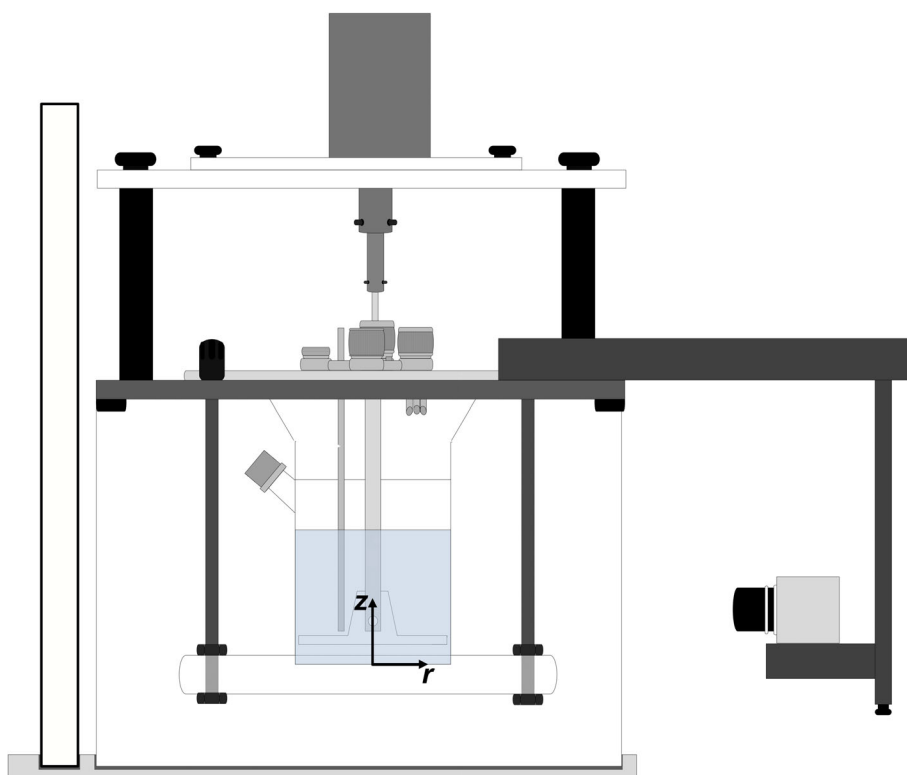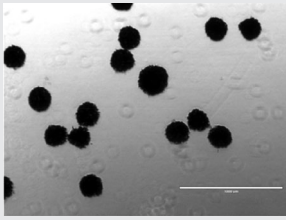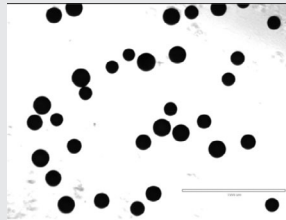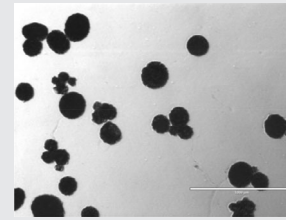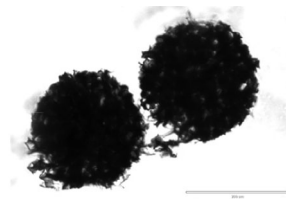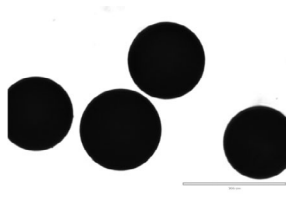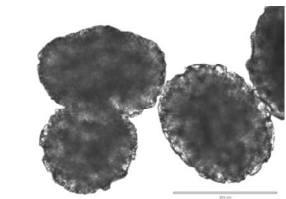

FIGURE 1 Experimental setup [Color figure can be viewed at wileyonlinelibrary.com]

TABLE 1 Diameter (D_{50}, D_5, D_{95}), density (ρ, $\rho_{s,eff}$), porosity (Φ) and inverted microscope images at 120 and ×600 magnification for three commercial microcarriers

	Cytopore 1	Cytodex 3	Cultispher-G
D_{50} (μm)	235	175	255
D_5, D_{95} (μm)	200, 270	130, 220	130, 380
ρ (g/cm^3)	1.03	1.04	1.04
Φ (%)	Macroporous >90%, (pore size 30 μm)	Non-porous/microporous	Macroporous ≈ 50%, (pore size 10–30 μm)
$\rho_{s,eff}$ (g/cm^3)	1.003	1.04	1.02
×120			
×600			

$$H(N) = \frac{1}{1 + e^{-a(N-x_0)}} \quad (4)$$

where parameters a and x_0 are found from a nonlinear regression analysis (R^2-squared fitting of >.95). This curve was then used to determine the minimum speed to reach full homogenization, N_H, when $H = 95\%$.

2.3 | Mixing time characterization experiments

Mixing time measurements were conducted using the same experimental set up for the suspension characterization (Figure 1) in the flat bottomed DASGIP bioreactor using a colorimetric acid base reaction technique: Dual Indicator System for Mixing Time.[23-26] To ensure experimental consistency, feed addition of the base was made from a fixed sample port in the bioreactor headplate (r/T = 0.4 from the impeller). Despite this, Samaras et al[25] have shown that mixing time experimental repeats can vary significantly (up to 55%) depending on the initial depth reached by base insertion (z/H_L > 0.65). It was found that more consistent mixing time measurements were obtained when the tracer reached lower depths, closer to the impeller. Therefore, in the rest of this work only experimental repeats corresponding to insertion depth z/H_L < 0.65 were considered. This allowed more consistent and reliable comparison between different sets of data obtained for a broad range of speeds and agitation modes.

Mixing time measurements were performed, investigating both continuous and intermittent agitation modes, for which 5 repeats per condition were completed. Continuous agitation modes were investigated at N = 75, 90, 105 and 120 rpm. Intermittent agitation modes were investigated at N = 90 rpm, T_{inv} = 30 s and T_{dwell} = 500–30,000 ms. The green hue of each image was post-processed using a purposely-written MATLAB code and the mixing time was determined when the SD of its distribution across the tank reached 5%, σ_G = 0.05.[23] Images were acquired at a frame rate of 2 Hz for 5 min for each experimental condition.

3 | RESULTS AND DISCUSSION

3.1 | Suspension characterization

The first part of this study aimed at characterizing the suspension for the two DASGIP bioreactor configurations operating under continuous agitation modes for three different commercially available MC types.

The variation of the homogeneity index, H and the corresponding fitted model, determined using Equations (3) and (4), respectively, for increasing rotational speeds is given in Figure 2 for the three MC types investigated in both the flat and round bioreactor configurations. A minimum rotational speed of N = 20 rpm is necessary to initiate suspension of Cytodex 3 and Cultispher-G, while Cytopore 1 already begin to suspend at an agitation speed of N = 10 rpm. As the rotational speed is further increased the degree of homogeneity improves. Non-porous (effective density, $\rho_{s,eff}$ = 1.04 g/cm^3) and small-sized (D_{50} = 175 μm) Cytodex 3 were found to reach system homogeneity, $H \geq 95\%$, at N_H = 37.6 rpm in the flat configuration. Cytopore 1, which have an effective density ($\rho_{s,eff}$ = 1.003 g/cm^3)

FIGURE 2   Variation of the degree of homogeneity, *H*, with increasing rotational speeds for different microcarrier and bioreactor combinations [Color figure can be viewed at wileyonlinelibrary.com]
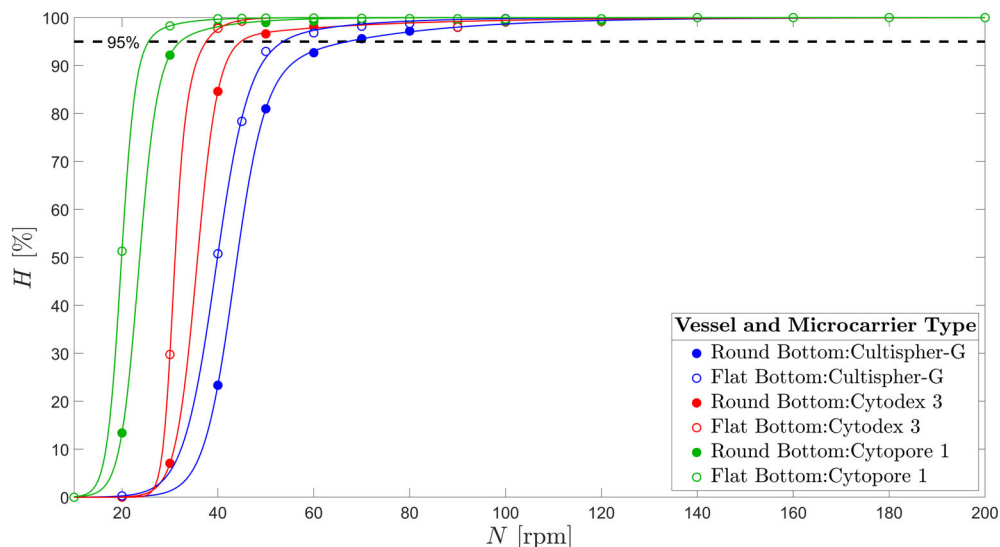

TABLE 2   Minimum speed to reach homogeneity (rpm), N_H, for different microcarrier and bioreactor combinations

Bottom configuration microcarrier type	Flat	Round
Cytopore 1	25.5	32.2
Cytodex 3	37.6	44.8
Cultispher-G	53.6	67

close to the working fluid (ρ = 1.00 g/cm^3), were found to fully suspend at the lowest rotational speed, N_H = 25.2 rpm. They are larger in size than Cytodex 3 (D_{50} = 235 μm), however the small reduction in effective density, only 3.6%, is enough to obtain an overall better suspension performance. In contrast, the reduction in effective density of Cultispher-G (1.9%), was not enough to outbalance the increase in size of the MCs, which are the least efficient to suspend, N_H = 53.6 rpm. The increase in suspension speed may also be related to the broader ranges of MC diameter and pore size of Cultispher-G, with D_{95} reaching values of 380 μm, nearly 50% greater than their nominal value (D_{50} = 255 μm). The same observations can be made for the round bottom configuration. When comparing suspension dynamics between the two bottom geometries, it is evident across all the datasets that the flat bottom configuration is more efficient at suspending. An approximate 16–22% increase in N_H was observed for all MCs in the round bottom configuration. This may be attributable to a number of factors, mainly the lower impeller clearance in the flat bottom geometry. The presence of the small dimple at the center of the tank would also have an impact which, according to Venkat et al[27] promotes suspension below the impeller. Indeed, the findings are consistent with the flow dynamics data presented in Part 1 of this work, where a stronger lower circulation loop and trailing vortex were observed in the flat bottom reactor. A summary of the measured N_H is provided in Table 2.

Figure 3a presents the dimensionless time/revolutions needed to fully suspend and reach 95% homogeneity, Nt_H, for increasing rotational speeds. In the figure two distinct regions can be observed for all

data sets: the first part shows an initial decay in number of revolutions to lift the MCs with increasing speed, whereas from approximately $N \geq 120$ rpm the number of revolutions to reach homogeneity becomes constant. This implies that a fixed number of revolutions is needed to lift the MC in each case, irrespective of the impeller speed. It is obvious from this figure that achieving suspension at the lowest speed does not necessarily imply a fast suspension rate. This is true, for example, observing Cytopore 1, which at 25.5 rpm fully suspend in approximately 25 revolutions (flat bottom geometry), while Cultispher-G at double the speed, 53.6 rpm, can be seen to fully suspend in approximately 18 revolutions. When comparing the curves of Cultispher-G and Cytodex 3, Cultispher-G is shown to consistently suspend faster with fewer revolutions from $N \geq 80$ rpm, however Cytodex 3 can suspend at speeds as low as 50 rpm, suggesting that once suspended Cultispher-G is more efficiently lifted. This may be attributed to the increase in MC porosity, which according to Equation (2), results in a reduction of the effective density of a particle. Applying Equation (2), the effective density for Cultispher-G is ≈ 1.02 g/cm^3 while for Cytodex 3 is 1.04 g/cm^3. This may suggest that the decrease in MC size, as previously highlighted, is more significant to suspend at lower speeds, however as the speed increases the impact of size becomes less relevant and the number of revolutions to lift becomes more affected by the difference in effective density/porosity. Overall, the flat bottom configuration is observed to suspend the MCs at lower rotational speeds with fewer revolutions

Based on these results, an agitation strategy with different speeds could potentially minimize the time taken to reach and sustain full suspension. For example, when considering Cytodex 3 in the flat bottom geometry (see Figure 3a) a high speed of 100 rpm could initially be used for a short period (~10 revolutions) to fully suspend all MCs, while a lower speed of 40 rpm could then be adopted to maintain suspension throughout the process, minimizing shear effects and power consumption. This strategy can be adopted for any combination of speeds, with $N > N_H$.
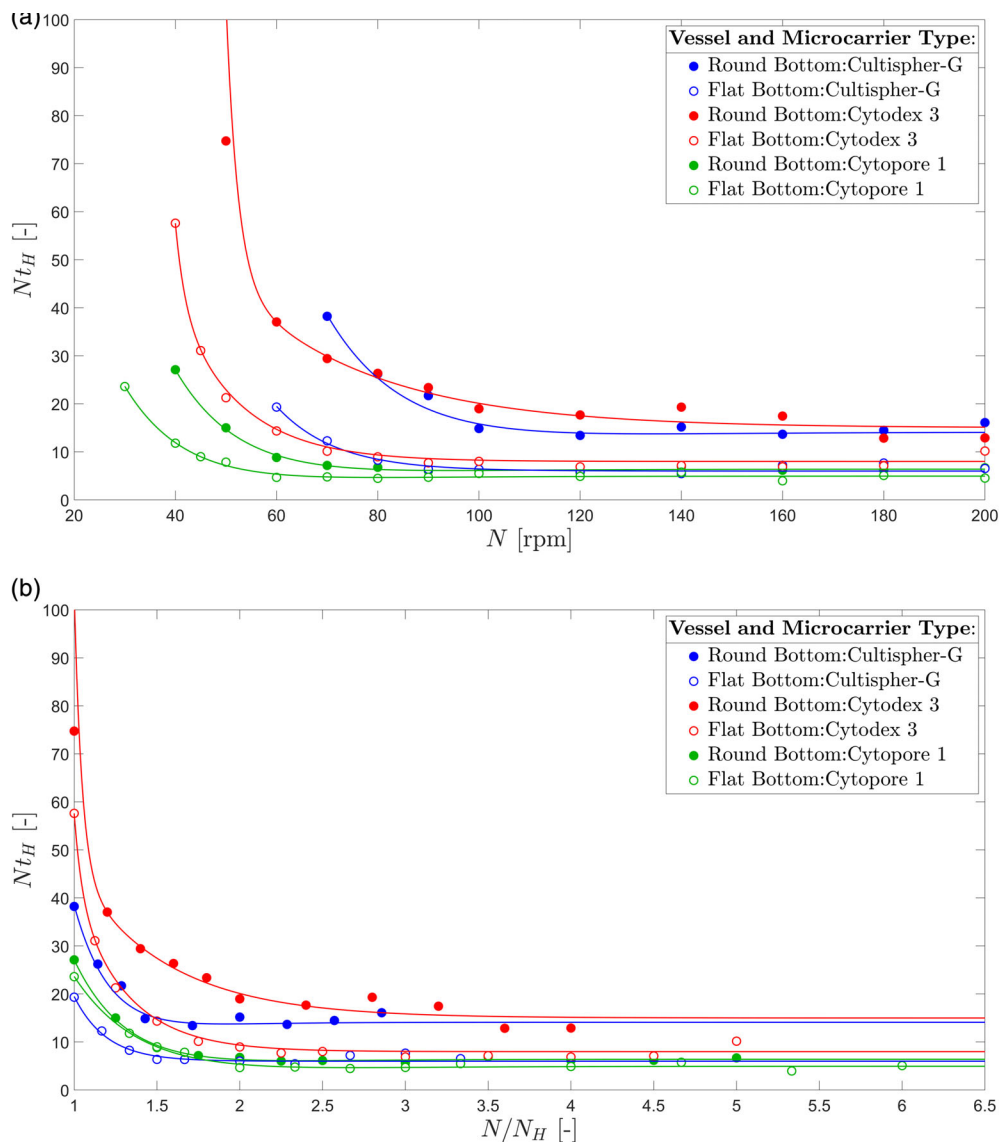
TABLE 3 The constant of number of revolutions, $(Nt_H)_0$, for different microcarrier and bioreactor combinations

Bottom configuration microcarrier type	Flat	Round
Cytopore 1	4.95	6.4
Cytodex 3	8	15
Cultispher-G	6	14.1

A further comparison of the final plateau between the different datasets can be gained from Figure 3b, where all rotational speeds are normalized against their corresponding minimum speed at which the system reaches a fully homogeneous distribution, N_H. In this case it is interesting to see that each MC curve plateaus for similar values of N/N_H in a relatively narrow range $1.5 < N/N_H < 2.5$. The constant number of revolutions, $(Nt_H)_0$, achieved for each MC-reactor configuration for $N/N_H > 2$ is summarized in Table 3. In general, it can be seen that for each MC type the flat bottom configuration suspends faster (i.e., lower number of revolutions).

Suspension dynamics for intermittent agitation conditions are considered in Figure 4a–c where the variation in time of the homogeneity index, H, for different dwell durations (T_{dwell} = 500–30,000 ms) is given for the three MCs tested, Cytopore 1, Cytodex 3 and Cultispher-G, respectively. All experimental data shown were conducted at N = 90 rpm, starting with the MCs fully settled at t = 0 s and the dwell phase initiation at t = 30 s. The numerical values reported in each plot were averaged from 10 experiments and correspond to the conditions denoted by an asterisk in the legend. As expected, the degree of settling increases linearly with T_{dwell}, after an initial non-linear phase. For the longest dwell duration (T_{dwell} = 30,000 ms) the degree of homogeneity, H, decreased the least for Cytopore 1 (Figure 4a), H_{min} = 89.6%, while Cytodex 3 and Cultispher-G settled to H_{min} = 79.5 and 34.6%, respectively. The largest, intermediate effective density and porosity MC, Cultispher-G, clearly exhibits the greatest variation of H in comparison to Cytodex 3 and Cytopore 1.
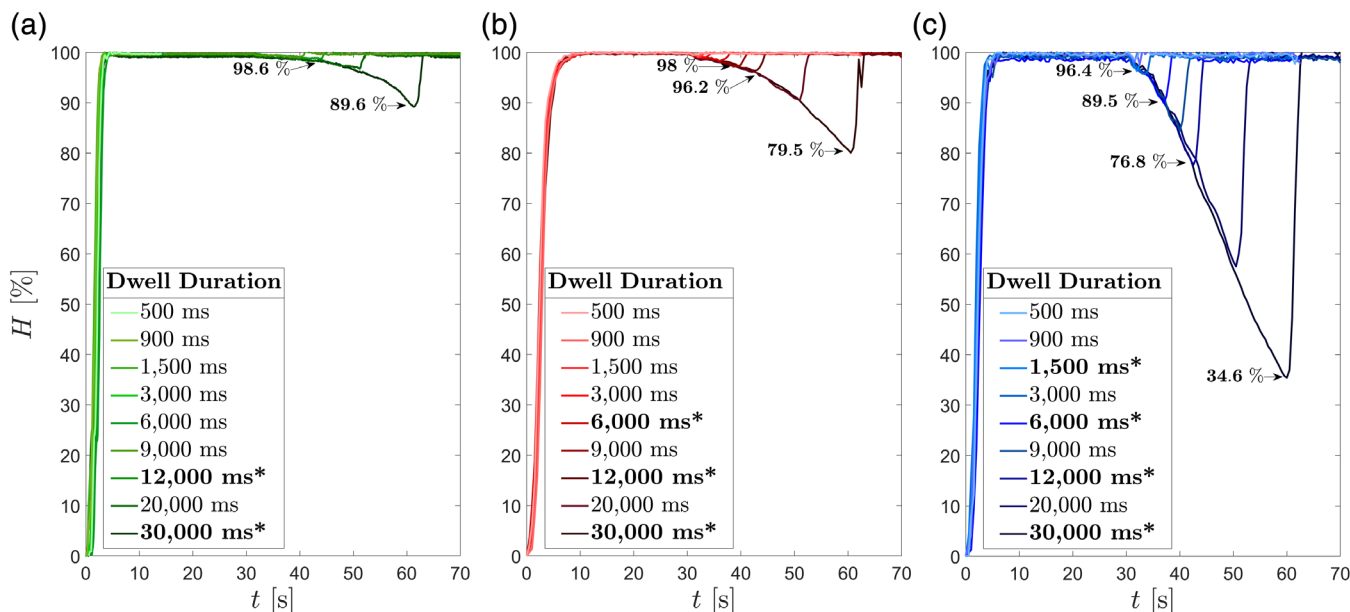
FIGURE 4 Variation of the degree of homogeneity for increasing dwell time with intermittent agitation, N = 90 rpm, T_{inv} = 30 s: (a) Cytopore 1; (b) Cytodex 3; (c) Cultispher-G [Color figure can be viewed at wileyonlinelibrary.com]

TABLE 4 Comparison of settling velocity, u_s, obtained from experimental data (bold values), manufacturer manuals and a corrected form of Stokes equation

	Average rate of settling (—)	Calculated u_s (cm/s)	Manufacturer u_s (cm/s)	Stokes's equation u_s (cm/s)
Cytopore 1	**0.0094**	**0.069–0.078**	0.216–0.3167[a]	0.2–0.24
Cytodex 3	**0.0114**	**0.073–0.077**	0.2–0.267[a]	0.6–0.78
Cultispher-G	**0.0227**	**0.138–0.172**	—	0.43–0.73

[a]Obtained from Reference 9.

Table 4 summarizes the rates of settling determined for each MC in the first column, while the corresponding settling velocity, u_s, was empirically determined by multiplying the settling rate and the MC height variation by the end of the dwell period. A comparison is then made with the settling velocities provided by the manufacturer in the third column and with settling velocities calculated from a corrected Stokes equation accounting for the effective density (Equation 5) in the final column.

$$u_{s,eff} = \sqrt{\frac{2\left(\left((1-\Phi)\rho_s + \Phi\rho_L\right) - \rho_L\right)gV}{C_D A \rho_L}} \qquad (5)$$

where A and V are the particle external surface and volume respectively, while C_D is the drag coefficient for a smooth sphere in turbulent flow. The volume and external surface were calculated using diameters, D_5–D_{95}, commonly provided by the manufacturer. It is evident that the settling velocities provided by the manufacturer and those obtained from Stokes equation tend to significantly overestimate the measured settling velocity (approximately threefold in the case of Cytopore 1, ninefold with Cytodex 3 and fourfold with Cultispher-G). It must be remarked that the Stokes equation is valid for a single particle settling in a stagnant fluid, these conditions are not valid for the current investigation.

Finally, it must be noted that when the agitation is resumed full resuspension occurs rapidly, t_r = 2–4 s, for all dwell times investigated. Similar to the suspension measurements, Cytopore 1 was the quickest to resuspend, while Cytodex 3 took the longest.

3.2 | Mixing dynamics

The second part of this study aimed at characterizing the mixing dynamics occurring within the flat bottom DASGIP configuration both for continuous and intermittent agitation modes. Mixing experiments were carried out in a single-phase configuration (i.e., without MCs), as Grein et al[17] showed that mixing characteristics for their reactor configuration were not affected by the presence of MCs for impeller rotational speeds >70 rpm.

Similar to the work of Rodriguez et al,[23,28] the variation in time of the SD across the measurement volume of the green channel, σ_G, was used to determine the mixing time (i.e., time corresponding to σ_G = 0.05). Figure 5a shows the variation of σ_G against the number of impeller revolutions, Nt, for the continuous agitation mode, N = 90 rpm. At the beginning of each experiment the SD of the green channel is zero (the system is homogeneous). It then rapidly increases
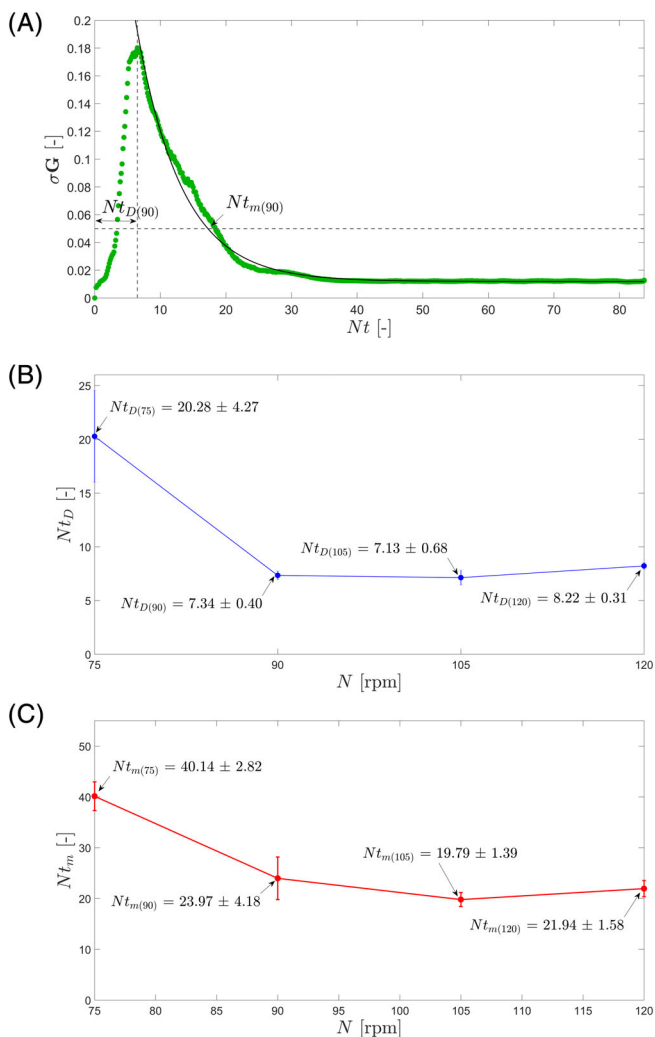
FIGURE 5 Variation of the degree of mixing for continuous agitation: (a) SD of the normalized green channel output, σ_G, at N = 90 rpm; (b) dispersion number, Nt_D, for N = 75, 90, 105 and 120 rpm; (c) mixing number, Nt_m, for N = 75, 90, 105 and 120 rpm [Color figure can be viewed at wileyonlinelibrary.com]

with the base insertion and a SD peak is reached which corresponds to the dispersion time, t_D, of the base and the initiation of the mixing process. From t_D onwards the SD decreases and plateaus at $\sigma_G \approx 0.0121$. This threshold corresponds to the maximum level of uniformity (i.e., minimum SD) which can be achieved with the current set up and is a measure of the systematic error related to a pixel by pixel difference in camera sensitivity. It was found to vary by ~10% (σ_G = 0.0111–0.0131) between experimental repeats. As shown in Figure 5a the final mixing time, t_m, was estimated by fitting an exponential decay curve through the data points for $t > t_D$ (i.e., from the SD peak) and by identifying the point corresponding to σ_G = 0.05.

Figure 5b,c show the dispersion number, Nt_D (B) and mixing number, Nt_m (C), for increasing rotational speeds, N = 75–120 rpm. As expected, the dispersion number and mixing number in Figure 5b,c are shown to decrease with rotational speed, indicating that fewer revolutions are required for the base to become fully dispersed/
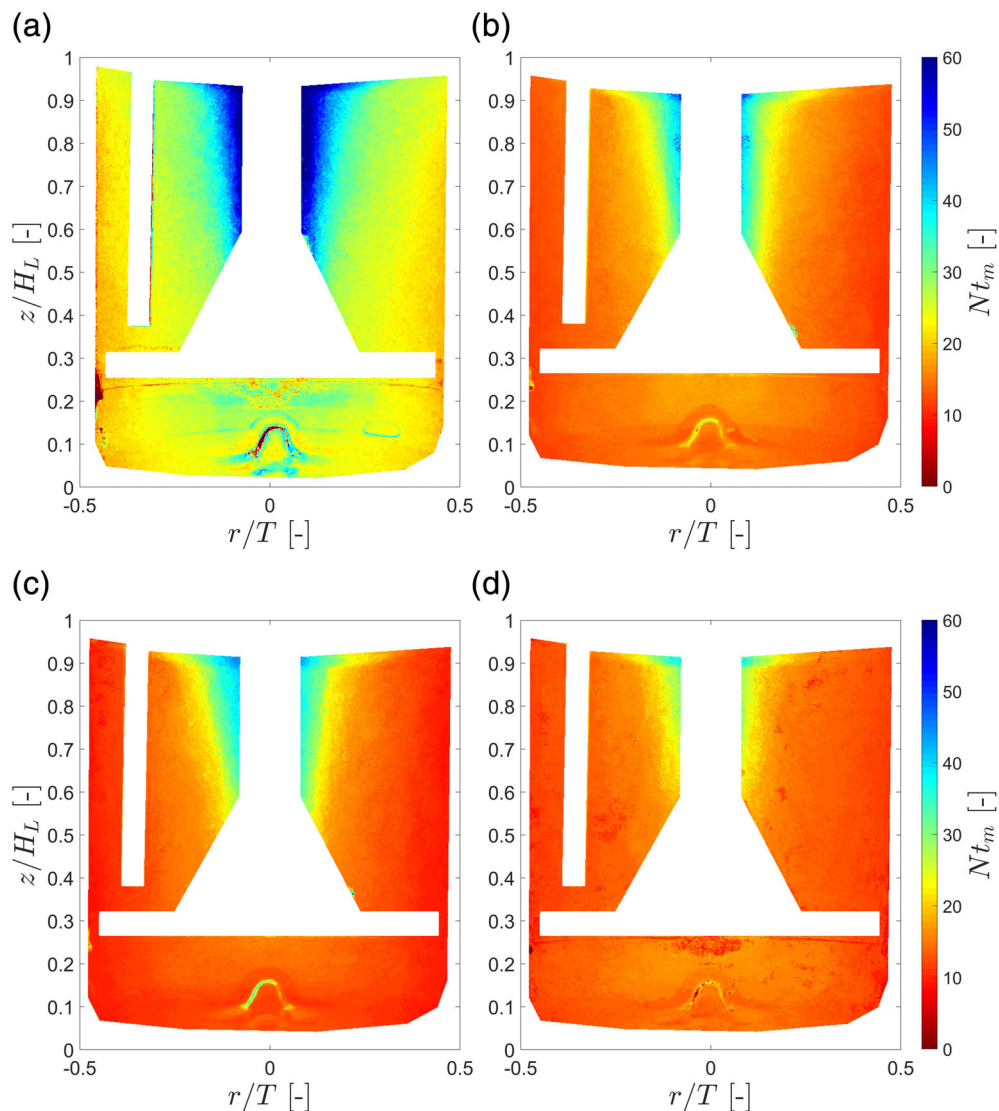
mixed. From Figure 5c it can be noticed that the mixing number plateaus for $N > 90$ rpm, with a percentage variation of 8.5% between N = 90 rpm (Re = 5,400) and 120 rpm (Re = 7,200). This implies that for this vessel configuration, turbulent conditions (i.e., constant mixing number) are reached at relatively low Reynolds (Re = 5,400). This seems to be consistent with the results obtained by Zhang et al,[29] who found Reynolds independent flow behaviour for $Re > 6,000$ in a small sized stirred tank vessel (T = 28.5 cm) equipped with a Rushton Turbine impeller. Similarly, Machado et al[30,31] also showed low Re associated to turbulent flow regimes for both axial and radial flow impeller types. Generally, lower ranges in Re have been associated with the turbulent flow transition as the impeller to tank diameter (D/T) ratio increases and with decreasing vessel size.[29-32] This is consistent with the flow dynamics data presented in Part 1 of this work, where flow velocities scaled well across the rotational speeds investigated (N = 75–120 rpm), suggesting the mean flow was fully developed and exhibits a turbulent regime

The mixing number for the impeller-reactor configuration investigated in this work is approximately Nt_m = 22. To put this into context, typical mixing numbers reported in the literature for an axial impeller range from Nt_m = 30–36.7 (N = 50–250 rpm and V_w = 1.5–2.5 L),[33-35] while Nt_m = 17–47 for a radial flow Rushton turbine impeller (V_w = 1–120 L and N = 50–2,165 rpm).[20,35-37] The current impeller-reactor configuration is in between these two types, as the flow it generates is mostly in the axial direction (see Part 1), despite the paddle being a radial impeller. The fill volume used in this work (V_w = 0.20 L) is considerably lower than those found in the literature, similarly, this configuration also has a much larger impeller D/T, which results in higher turbulence levels ($\bar{U}'/V_{tip}$ = 0.1). A reduction in mixing number is therefore expected[17,29,30,33] and as such the determined mixing number in this work ($Nt_m \approx 22$) is most consistent with performance observed for an axial flow impeller, (Nt_m = 30–37).

To spatially observe the mixing dynamics within the reactor, the local mixing number map, reconstructed from the average of five experimental repeats, is shown in Figure 6a–d, for rotational speeds N = 75–120 rpm. All maps show a region of slower mixing around the impeller shaft at the top of the tank. The swirling motion induced by the rotation of the impeller causes entrapment of the acidic fluid close to the shaft with limited mass transfer with the rest of the reactor. The non-dimensional mixing times in this region are $\approx$ 4–7-fold higher than those closest to the bioreactor wall and within the impeller region. This is in agreement with the flow characterization provided in Part 1 of this work, which showed that regions of higher shear occur at the interfaces between the trailing vortices and at the bioreactor walls. When comparing mixing maps for increasing rotational speed (Figure 6a–d), the slow mixing region is found to decrease in size but with nearly unaltered mixing number (25 < Nt_m < 35), while Nt_m decreases significantly in the bulk volume (reduced by half).

Using a threshold value of Nt_m = 18, it was possible to distinguish between the fast and slow mixing regions and evaluate each independently. Overall, there is an increase in size of the fast mixing region from 78 to 96% the total volume when the speed is increased from 75 to 120 rpm. Conversely, the slow mixing region shows an 81%

FIGURE 6 Average mixing number map for increasing continuous rotational speeds: (a) N = 75 rpm; (b) N = 90 rpm; (c) N = 105 rpm; (d) N = 120 rpm [Color figure can be viewed at wileyonlinelibrary.com]

decrease in size with increasing N. This influence is well captured in the SD variation shown in Figure 7a,b for N = 75 rpm and 120 rpm, where the fast and slow mixing regions and the entire reactor volume are denoted by blue, red and green hues, respectively. For the lower rotational speed (Figure 7a), the SD profile of the slow mixing region takes a longer time to disperse the tracer, reaching a maximum at Nt = 30, while the other two curves reach a peak at Nt = 23. This aspect is found to impact on the final mixing number, Nt = 47, of the entire vessel (green line), which is higher than the value associated to the fast mixing region, Nt = 40. When the rotational speed is increased (Figure 7b), the data points for the entire vessel volume and fast mixing region nearly overlap throughout the time range investigated, indicating that the size of the slow mixing region (4% at this speed) is much smaller and does not influence the final estimate of the mixing time.

To observe the variation of the mixing map occurring between five experimental repeats, the SD of the mixing number achieved in each pixel, σ_{Ntm}, was used to construct the maps observed in Figure 8a–d for increasing rotational speeds, N = 75–120 rpm. In this

plot high values of SD indicate regions subject to large variation between repeats. For all the rotational speeds considered, the region of highest SD occurs close to the impeller shaft, in the region denoted as "slow mixing" in Figure 6. Mixing time repeatability is therefore mainly affected by and confined to the region of solid body rotation present around the shaft.

Intermittent agitation experiments and the corresponding mixing time are reported in Figures 9 and 10. Figure 9a shows the mixing time curve for N = 90 rpm, T_{inv} = 30 s and T_{dwell} = 9,000 ms, where the dwell occurs in the middle of the mixing process and begins/ends at 4.3/13.3 s. A visualization of the timing of tracer insertion with respect to the dwell phase is provided in the inset of Figure 9a,b where "ON" and "OFF" agitation conditions are clearly shown. To better compare with the shear stress data of figure 12 in Part 1, the two asterisk symbols represent the observed spike in shear rate at the start and end of the dwell phase. For reference purposes the curve associated to continuous agitation (green) is also shown. Insets numbered from 1 to 6 with the corresponding time instants indicated on the curve are shown to better visualize the mixing process. Following
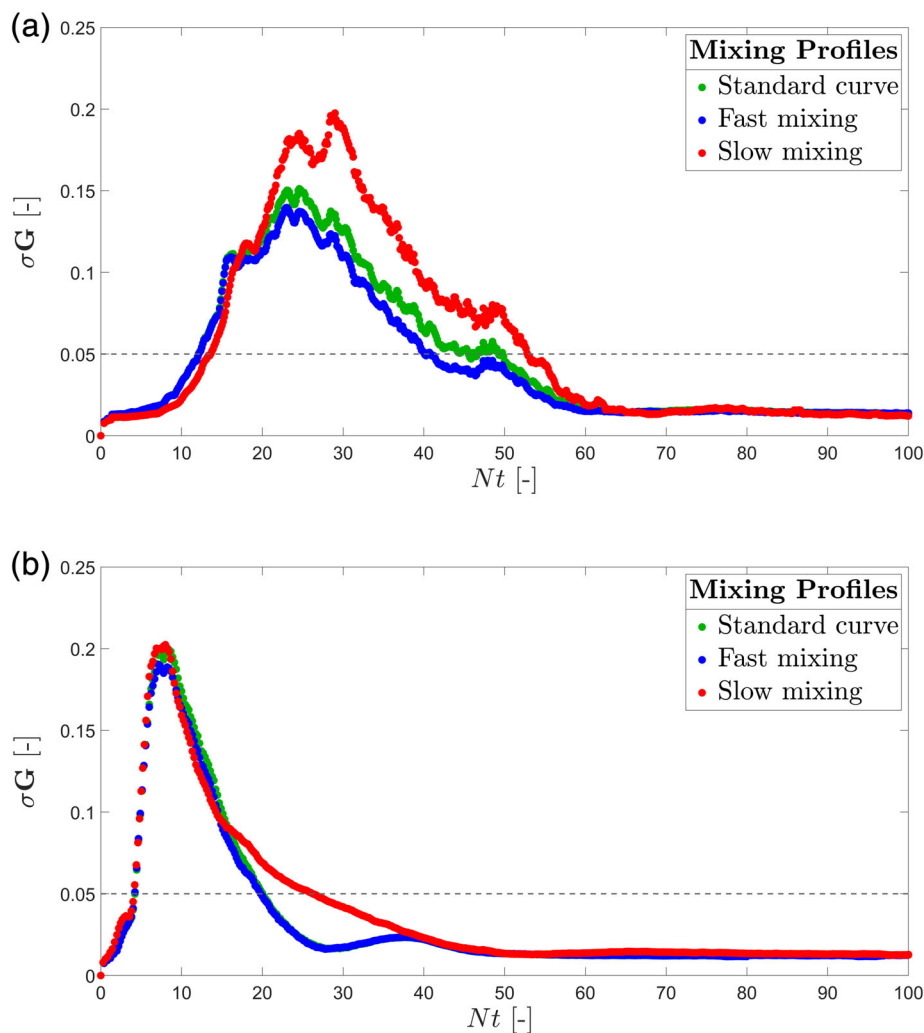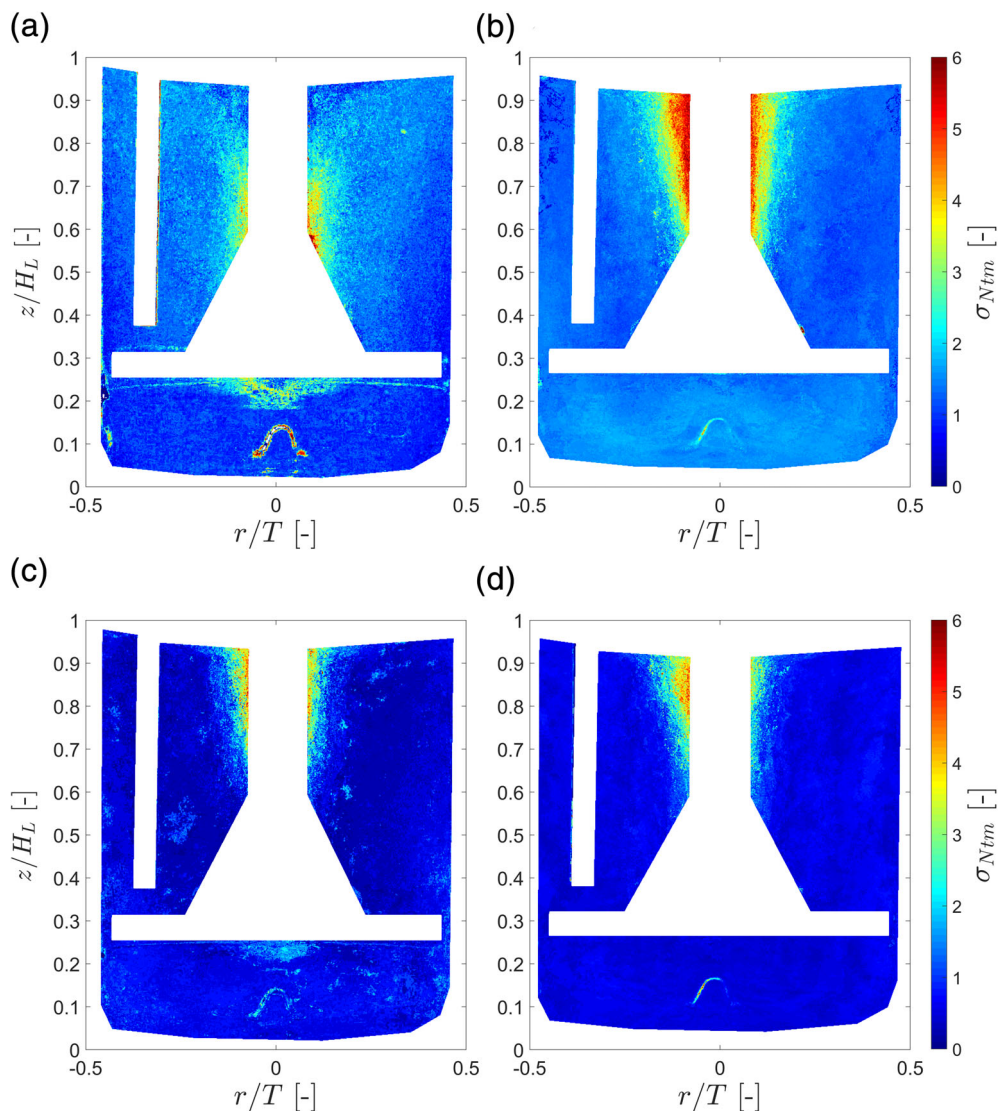
(a)

(b)

FIGURE 7 Segregation of fast and slow mixing regions using the threshold $Nt_m = 18$: (a–b) *SD* profiles of the normalized green channel in the segregated fast mixing (blue) and slow mixing (red) regions with the overall (green). (a) $N = 75$ rpm; (b) $N = 120$ rpm [Color figure can be viewed at wileyonlinelibrary.com]

dispersion of the tracer (Image 2), the mixing process follows from $t > t_D$. The rate of mixing can be seen to be nearly constant for the continuous agitation (green curve), whilst for the intermittent case three distinct regions of the curve can be observed. The initial rate of mixing between Images 2 and 3 is higher than for continuous agitation, suggesting improved, faster mixing as a result of the small transient spike in shear at the start of the dwell (first asterisk on the inset, discussed in Part 1). A noticeable variation in the rate of mixing can then be observed after Image 3, when the two curves exhibit a nearly parallel rate of decay (up to Image 4). This time range corresponds to the gradual loss of inertia of fluid motion following the initial shear spike. Approximately 8 s into the dwell period, the mixing within the bioreactor begins to substantially slow (Images 4–5) as fluid transport across the reactor is significantly limited (at this speed full static conditions are achieved approximately after 12 s following the start of dwell). The restart in impeller motion at the end of the dwell phase coincides with a second, more significant spike in shear rate (second asterisk on the inset, previously discussed in Part 1), associated with another rapid rate of decay in the mixing profile (Images 5 and 6). The difference between the time of dispersion for the continuous and intermittent profiles is possibly due to the different initial depth

reached in each experiment by the tracer after addition. In fact, this is within the variation observed over experimental repeats, $n = 5$ for the continuous agitation mode. As a consequence, it cannot be conclusively argued that the total mixing time variation shown in Figure 9a is completely related to the different agitation strategy selected. It could also be correlated with increase in dispersion time due to the depth of insertion. This data highlights that when the mixing process is initiated before the dwell phase the benefit from the spikes in shear/velocity, observed at the stop and restart of the impeller, could be outbalanced by the loss of momentum during the dwell phase.

Figure 9b considers the impact of dwell duration on the mixing process when tracer insertion time coincides with the restart of the impeller motion (i.e., end of the previous dwell). The plot of Figure 9b indicates dispersion and mixing directly after restart of the impeller motion, thus exploiting the impact of the second, more intense spike in shear rate and velocity magnitudes identified in the flow analysis, Part 1 of this paper. This second spike following the restart in impeller motion was shown to linearly increase with dwell duration until a plateau in the spike was observed when fully static flow was achieved during the dwell ($T_{dwell} = 12,000–30,000$ ms). The rate of dispersion of the mixing profiles in Figure 9b increases with increasing dwell

FIGURE 8 *SD* of the average mixing number maps for continuous increasing rotational speeds: (a) *N* = 75 rpm; (b) *N* = 90 rpm; (c) *N* = 105 rpm; (d) *N* = 120 rpm [Color figure can be viewed at wileyonlinelibrary.com]

duration: T_{dwell} = 1,500–30,000 ms, gradient 0.02–0.03, thus with the increasing magnitude of the second spike in shear. As expected, similar dispersion occurs when the flow is fully static before impeller motion (T_{dwell} = 20,000 and 30,000 ms)

From the analysis of Figure 9a,b, the moment of insertion with respect to the timing of the dwell phase should be carefully considered to maximize the improvement of the mixing time. Figure 9a shows a general case, where the dwell is occurring in the middle of the mixing process and no significant improvement in mixing time is attained between intermittent and continuous agitation. In contrast, Figure 9b shows when base insertion is synchronized with the end of the dwell phase, full use is made of the larger spike in shear rate and velocity magnitude occurring at the impeller restart, without compromising with the loss of inertia registered in the dwell phase. Based on this data, the best insertion strategy corresponds to timing the tracer feed with the restart of the impeller after the dwell phase such as to fully exploit the second more intense spike observed in shear rate.

The overall mixing number is shown in Figure 10a for increasing dwell durations, T_{dwell} = 500–30,000 ms, where tracer addition in

each case is made at the end of the dwell phase. The mixing number achieved during continuous agitation is included for reference ($Nt_{m[90]}$ = 23.97). According to the results presented in Part 1, the fluid conserves some inertia for at least one period of revolution during the dwell phase (667 ms), while full static flow conditions are reached after ~12 s (at 90 rpm). This suggests that for T_{dwell} = 500 ms there is little deceleration in fluid motion, however the mixing number is shown to reduce by ~28% with respect to the continuous agitation mode. This can be attributed to the two spikes in shear rate introduced at the start (+ 5%) and end (+ 20%) of the dwell phase, with little loss in flow inertia and transport. As T_{dwell} is further increased, flow inertia and thus mixing efficiency decays, however this aspect is partially counterbalanced by the mixing improvement generated by the second spike in shear after agitation is restarted, which is more pronounced for longer dwell times.

A final comparison of the mixing number (B) and *SD* (C) mixing maps for both continuous (left, *N* = 90 rpm) and intermittent (right, *N* = 90 rpm, T_{inv} = 30 s and T_{dwell} = 500 ms) agitation is made in Figure 10. The significant drop in mixing number, as previously

(a)

(b)
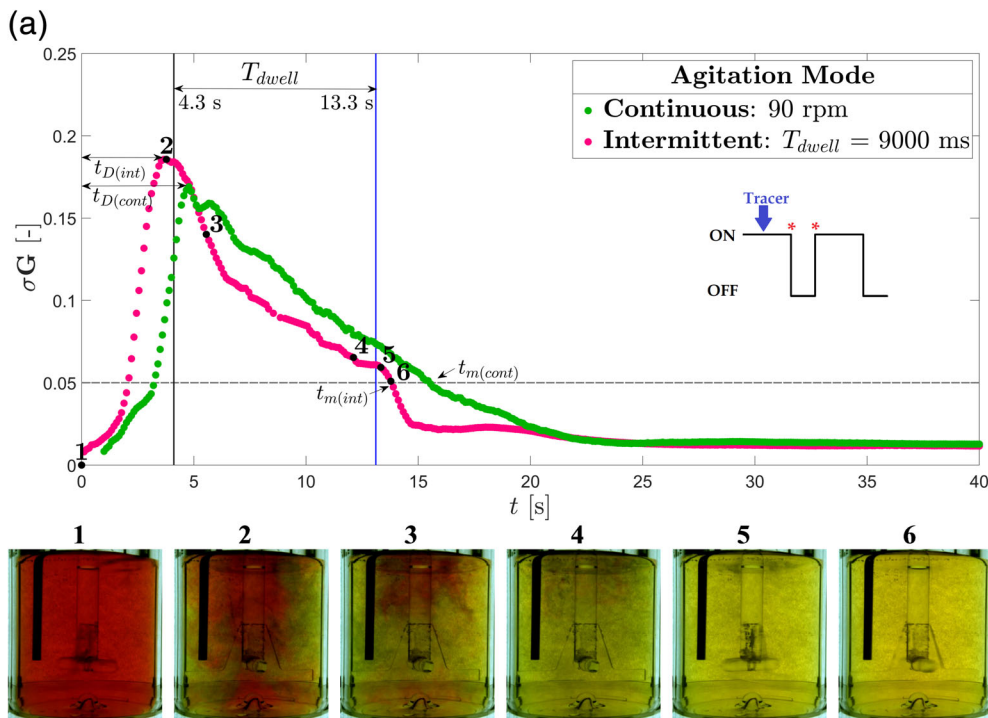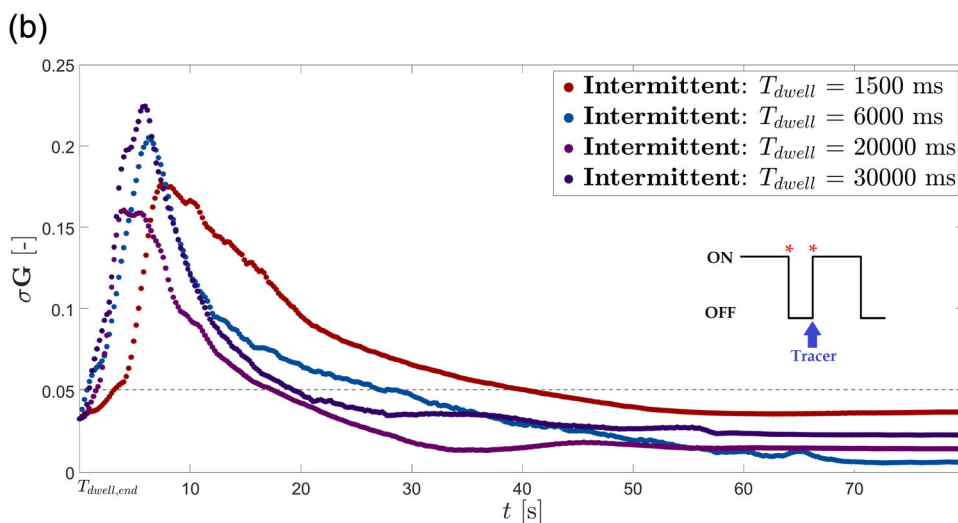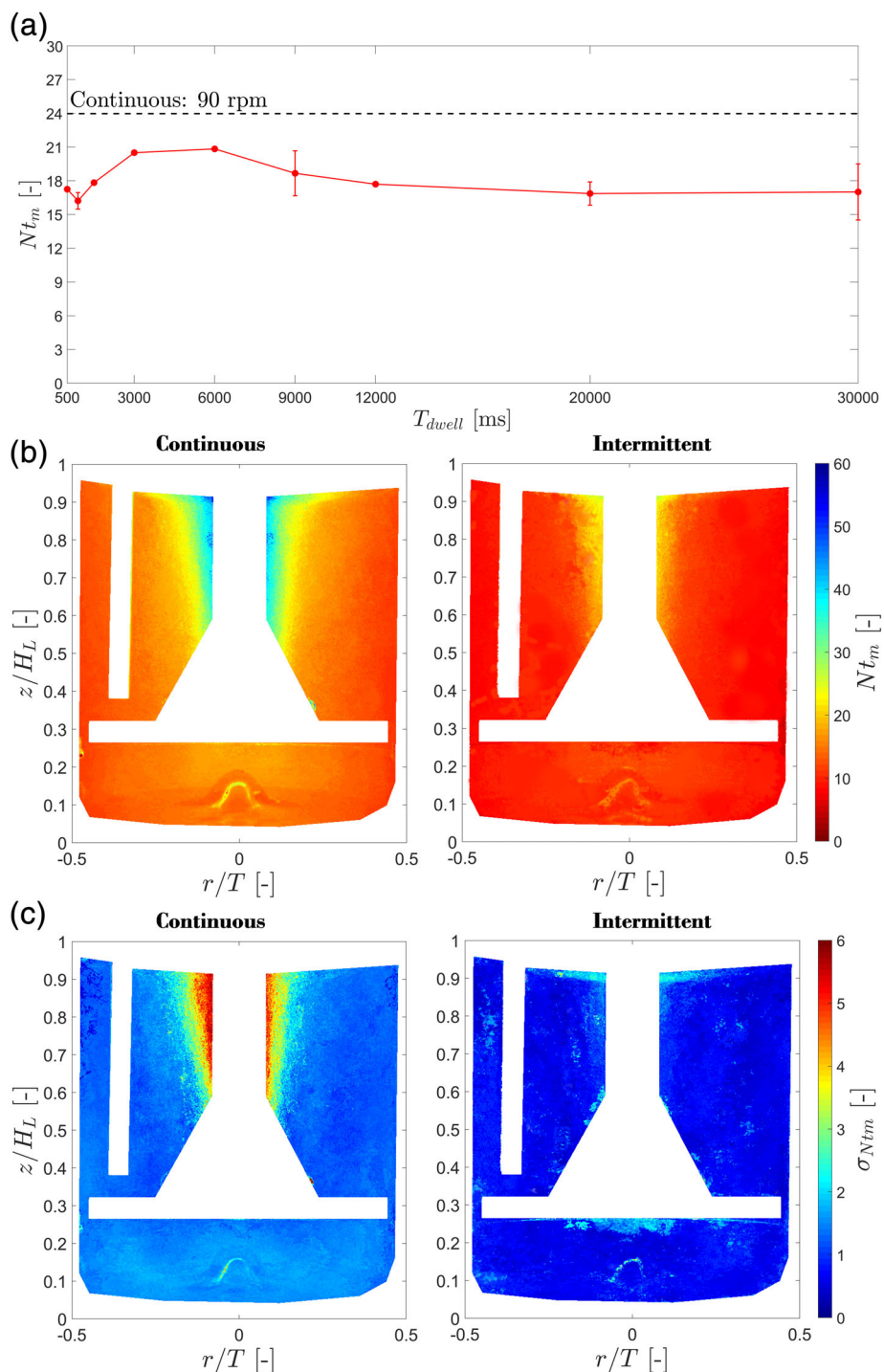

discussed for Figure 10a, is immediately evident in Figure 10b,c shows the level of *SD* is significantly reduced with intermittent agitation (right). Most noticeable is the apparent absence of the region of "slow mixing," identified previously. This suggests that the introduction of intermittent agitation breaks up the region of entrainment and entrapment around the impeller and faster macro-mixing times are observed.

To assess the impact of continuous and intermittent agitation strategies on power, the space-averaged maximum local shear rate, γ^{**}, and velocity magnitude, U_{rz}^{**}, calculated from Part 1 of this work, were averaged over one cycle, including both a motion and a dwell phase ($T_{inv} + T_{dwell}$). These two quantities can be used as a basic power indicator to assess the system efficiency for the two agitation strategies adopted. This data is summarized in Table 5. Taking the

continuous agitation mode as a reference, it is worth to point out that dwell times in the range T_{dwell} = 500–1,500 ms (italic values), showed higher values of both averaged shear rate and velocity magnitude, implying that a greater amount of power was used. This is also reflected in faster mixing times (see Table 5). The average values of shear rate and velocity magnitude associated with the continuous agitation mode are most similar to those obtained at T_{dwell} = 3,000 ms (bold values). Nevertheless, the mixing time of the intermittent agitation strategy still outperforms by 30% that for continuous agitation mode. Further increase in dwell time duration, T_{dwell} > 1,500 ms, resulted in a decrease in both shear rate and velocity magnitudes. Despite this, the overall mixing times for intermittent agitation remained favorable over continuous agitation (t_m = 12.1 ± 1.1 s and 16 s, respectively). Overall, the current results indicate that carefully

FIGURE 10 Variation of the degree of mixing for continuous and intermittent agitation: (a) mixing number, Nt_m, for N = 90 rpm, T_{inv} = 30 s and T_{dwell} = 0–30,000 ms when tracer addition is made close to the end of the dwell; (b) average local mixing number maps for continuous (left, N = 90 rpm) and intermittent (right, N = 90 rpm, T_{inv} = 30 s and T_{dwell} = 500 ms) agitation modes; (c) SD of mixing number maps [Color figure can be viewed at wileyonlinelibrary.com]

selected intermittent agitation conditions (T_{dwell} > 1,500 ms) should be recommended as they favor breakup of slow mixing regions in proximity to the shaft, resulting in a significant improvement of mixing efficiency. From the basic analysis carried out in this work using space averages of shear rate and velocity, it seems that power consumption is not significantly affected by the agitation strategy. Having said this, rigorous power number measurements are called for to fully assess the impact of intermittent agitation on power consumption in small scale reactors. To fully exploit the shear stress spike occurring at the

impeller restart, feed insertion should be synchronized with the end of a dwell phase.

4 | CONCLUSIONS

Having investigated the flow dynamics in Part 1 of this publication, the suspension and mixing dynamics were then studied in detail. In agreement with the flow characterization studies, it was found that

TABLE 5 Average shear rate (γ^{**}) and velocity magnitude (U_{rz}^{**}) across the bioreactor volume over one cycle, considered as $T_{inv} + T_{dwell}$, and mixing time (t_m) for continuous agitation, N = 90 rpm, and intermittent agitation, N = 90 rpm, T_{inv} = 30 s and T_{dwell} = 500–30,000 ms

T_{dwell} (ms)	γ^{**} (−)	U_{rz}^{**} (−)	t_m (s)
0 (continuous)	**0.295**	**0.0271**	**15.98**
500	*0.372*	*0.0329*	*11.5*
900	*0.350*	*0.0316*	*10.81*
1,500	*0.355*	*0.0312*	*11.89*
3,000	**0.289**	**0.0250**	**13.67**
6,000	0.217	0.0193	13.89
9,000	0.184	0.0166	12.44
12,000	0.142	0.0128	11.8
20,000	0.105	0.0095	11.24
30,000	0.074	0.0067	11.34

the flat bottom configuration of the DASGIP bioreactor resulted in more favorable suspension characteristics. A comparison was made between three commercially available MC types, where it was found that both effective density and size influence suspension dynamics, with opposing effects. A homogeneity-time constant, $(Nt_H)_0$, was observed for each MC combination which can be used to predict the minimum number of revolutions to achieve homogeneity for $N/N_H > 2$. Based on the data presented it can be suggested that selection of either small and compact MCs or those with a very low effective density should be considered for biological culture where lower operating speeds are desirable. Caution should also be exercised when MC size is less consistent, with broad variations of diameter and pore dimension.

Settling characterization during intermittent agitation modes showed a constant rate of settling for each MC type investigated and highlighted the need for further revision of theoretical models using Stokes equation when considering MCs' suspension characteristics. The differences in physical properties of the MCs, that is, size, porosity and effective density, were shown to vary the suspension/settling profile during intermittent agitation. This highlights the need for consideration of suspension dynamics, for example, over the course of a cell differentiation process, when morphological characteristics of MCs or EB evolve over time.

Section 3.2 of this work characterized the mixing dynamics within the flat bottom DASGIP bioreactor, operating under continuous agitation. It was found that the mixing number reached a plateau between N = 90 and 120 pm, suggesting a fully turbulent flow regime at Re = 5,400–7,200. Considering the large impeller to tank diameter ratio, D/T = 0.97, and the vessel fill volume and small reactor size, turbulence at low Re is expected and the characterized mixing number, Nt_m = 22, was found to be most comparable with axial flow impellers. Spatial assessment of the mixing number showed a region of entrainment and slow mixing around the impeller shaft, which caused a high level of variation between measurements. The influence of this slow mixing region upon mixing time was found to reduce with rotational speed from 22% the total volume to 4% at N = 75–120 rpm.

The introduction of intermittent agitation showed a beneficial impact upon the mixing processes within the bioreactor. The two observed spikes for the shear rate and velocity magnitudes, characterized in Part 1 of this publication, were demonstrated to have a tangible impact upon the mixing profile, however the timing of feed insertion with respect to the dwell phase affects the extent of mixing enhancement this may have. As dwell duration was increased, two flow conflicting elements affecting the final mixing time were apparent: the decay in mixing efficiency due to the flow deceleration, which is more pronounced for increasing T_{dwell}; and the improvement of mixing due to the increase in spike intensity of the shear rate with the restart in impeller motion after the dwell phase. When feed insertion is timed with the end of the dwell, fully exploiting the second, more intense spike in shear rate and velocity, mixing was shown to be improved. This impact can be maximized with the larger spike intensities associated to longer dwell durations, which also have the added benefit of reduced power input overall into the system. The introduction of intermittent agitation was shown to break up the slow mixing region around the impeller shaft, resulting in a significant reduction in SD between experimental repeats. Such observed results in the use of intermittent agitation are essential towards the design of processes adopting such strategies for optimization of MC-based cultivation processes.

ACKNOWLEDGMENTS

ORCID

Jasmin J. Samaras https://orcid.org/0000-0001-5668-4569
Martina Micheletti https://orcid.org/0000-0001-5147-0182

REFERENCES

1. Lara AR, Galindo E, Ramirez OT, Palomares LA. Living with heterogeneities in bioreactors. *Mol Biotechnol*. 2006;34(3):355-381. https://doi.org/10.1385/mb:34:3:355.
2. Zwietering TN. Suspending of solid particles in liquid by agitators. *Chem Eng Sci*. 1958;8(3–4):244-253. https://doi.org/10.1016/0009-2509(58)85031-9.
3. Armenante PM, Nagamine EU, Susanto J. Determination of correlations to predict the minimum agitation speed for complete solid suspension in agitated vessels. *Can J Chem Eng*. 1998;76(3):413-419. https://doi.org/10.1002/cjce.5450760310.
4. Ibrahim S, Nienow AW. Suspension of microcarriers for cell culture with axial flow impellers. *Chem Eng Res Des*. 2004;82(9):1082-1088. https://doi.org/10.1205/cerd.82.9.1082.44161.
5. Ibrahim S, Jasnin SN, Wong SD, Baker IF. Zwieterings equation for the suspension of porous particles and the use of curved blade impellers. *Int J Chem Eng*. 2012;2012:1-13. https://doi.org/10.1155/2012/749760.

6. Correia C, Serra M, Espinha N, et al. Combining hypoxia and bioreactor hydrodynamics boosts induced pluripotent stem cell differentiation towards cardiomyocytes. *Stem Cell Rev*. 2014;10(6):786-801. https://doi.org/10.1007/s12015-014-9533-0.

7. Samaras JJ, Abecasis B, Serra M, Ducci A, Micheletti M. Impact of hydrodynamics on iPSC-derived cardiomyocyte differentiation processes. *J Biotechnol*. 2018;287:18-27. https://doi.org/10.1016/j.jbiotec.2018.07.028.

8. Bianchi F, Malboubi M, Li Y, et al. Rapid and efficient differentiation of functional motor neurons from human iPSC for neural injury modelling. *Stem Cell Res*. 2018;32(May):126-134. https://doi.org/10.1016/j.scr.2018.09.006.

9. GE Healthcare Life Sciences. *Microcarrier Cell Culture: Principles and Methods*; 2013. https://www.gelifesciences.co.kr/wp-content/uploads/2016/07/023.8_Microcarrier-Cell-Culture.pdf. Accessed March, 2020.

10. Rafiq QA, Coopman K, Nienow AW, Hewitt CJ. Systematic microcarrier screening and agitated culture conditions improves human mesenchymal stem cell yield in bioreactors. *Biotechnol J*. 2016;11(4):473-486. https://doi.org/10.1002/biot.201400862.

11. Nienow AW, Hewitt CJ, Heathman TRJ, et al. Agitation conditions for the culture and detachment of hMSCs from microcarriers in multiple bioreactor platforms. *Biochem Eng J*. 2016;108:24-29. https://doi.org/10.1016/j.bej.2015.08.003.

12. Collignon ML, Delafosse A, Crine M, Toye D. Axial impeller selection for anchorage dependent animal cell culture in stirred bioreactors: methodology based on the impeller comparison at just-suspended speed of rotation. *Chem Eng Sci*. 2010;65(22):5929-5941. https://doi.org/10.1016/j.ces.2010.08.027.

13. Dos Santos F, Andrade PZ, Eibes G, da Silva CL, Cabral JMS. Ex vivo expansion of human mesenchymal stem cells on microcarriers. *Methods Mol Biol*. 2011;698:189-198. https://doi.org/10.1007/978-1-60761-999-4_15.

14. Fernandes AM, Marinho PAN, Sartore RC, et al. Successful scale-up of human embryonic stem cell production in a stirred microcarrier culture system. *Braz J Med Biol Res*. 2009;42(6):515-522. https://doi.org/10.1590/s0100-879x2009000600007.

15. Ting S, Chen A, Reuveny S, Oh S. An intermittent rocking platform for integrated expansion and differentiation of human pluripotent stem cells to cardiomyocytes in suspended microcarrier cultures. *Stem Cell Res*. 2014;13(2):202-213. https://doi.org/10.1016/j.scr.2014.06.002.

16. Steiros K, Bruce PJK, Buxton ORH, Vassilicos JC. Effect of blade modifications on the torque and flow field of radial impellers in stirred tanks. *Phys Rev Fluids*. 2017;2(9):1-18. https://doi.org/10.1103/PhysRevFluids.2.094802.

17. Grein TA, Leber J, Blumenstock M, et al. Multiphase mixing characteristics in a microcarrier-based stirred tank bioreactor suitable for human mesenchymal stem cell expansion. *Process Biochem*. 2016;51(9):1109-1119. https://doi.org/10.1016/j.procbio.2016.05.010.

18. Ozturk SS. Engineering challenges in high density cell culture systems. *Cytotechnology*. 1996;22(1–3):3-16. https://doi.org/10.1007/BF00353919.

19. Langheinrich C, Nienow AW. Control of pH in large-scale, free suspension animal cell bioreactors: alkali addition and pH excursions. *Biotechnol Bioeng*. 1999;66(3):171-179. https://doi.org/10.1002/(SICI)1097-0290(1999)66:3<171::AID-BIT5>3.0.CO;2-T.

20. Ducci A, Yianneskis M. Vortex tracking and mixing enhancement in stirred processes. *AIChE J*. 2007;53(2):305-315.

21. Doulgerakis Z, Yianneskis M, Ducci A. On the interaction of trailing and macro-instability vortices in a stirred vessel-enhanced energy levels and improved mixing potential. *Chem Eng Res Des*. 2009;87(4):412-420. https://doi.org/10.1016/j.cherd.2008.12.019.

22. Olmos E, Loubiere K, Martin C, Delaplace G, Marc A. Critical agitation for microcarrier suspension in orbital shaken bioreactors: experimental study and dimensional analysis. *Chem Eng Sci*. 2015;122:545-554. https://doi.org/10.1016/j.ces.2014.08.063.

23. Rodriguez G, Anderlei T, Micheletti M, Yianneskis M, Ducci A. On the measurement and scaling of mixing time in orbitally shaken bioreactors. *Biochem Eng J*. 2014;82:10-21. https://doi.org/10.1016/j.bej.2013.10.021.

24. Cabaret F, Bonnot S, Fradette L, Tanguy PA. Mixing time analysis using colorimetric methods and image processing. *Ind Eng Chem Res*. 2007;46(14):5032-5042.

25. Samaras JJ, Ducci A, Micheletti M. Suspension and mixing characterization of intermittent agitation modes in DASGIP bioreactors. *Chem Eng Technol*. 2019;42(00):1-8. https://doi.org/10.1002/ceat.201900069.

26. Melton LA, Lipp CW, Spradling RW, Paulson KA. DISMT—Determination of mixing time through color changes. *Chem Eng Commun*. 2002;189(3):322-338. https://doi.org/10.1080/00986440212077.

27. Venkat RV, Stock LR, Chalmers JJ. Study of hydrodynamics in microcarrier culture spinner vessels: a particle tracking velocimetry approach. *Biotechnol Bioeng*. 1996;49(4):456-466.

28. Rodriguez G, Weheliye W, Anderlei T, Micheletti M, Yianneskis M, Ducci A. Mixing time and kinetic energy measurements in a shaken cylindrical bioreactor. *Chem Eng Res Des*. 2013;91(11):2084-2097. https://doi.org/10.1016/j.cherd.2013.03.005.

29. Zhang Y, Gao Z, Li Z, Derksen JJ. Transitional flow in a Rushton turbine stirred tank. *AIChE J*. 2017;63(8):3610-3623. https://doi.org/10.1002/aic.15809.

30. Machado MB, Bittorf KJ, Roussinova VT, Kresta SM. Transition from turbulent to transitional flow in the top half of a stirred tank. *Chem Eng Sci*. 2013;98:218-230. https://doi.org/10.1016/j.ces.2013.04.039.

31. Machado MB, Kresta SM. The confined impeller stirred tank (CIST): a bench scale testing device for specification of local mixing conditions required in large scale vessels. *Chem Eng Res Des*. 2013;91(11):2209-2224. https://doi.org/10.1016/j.cherd.2013.06.025.

32. Mendoza F, Bañales AL, Cid E, et al. Hydrodynamics in a stirred tank in the transitional flow regime. *Chem Eng Res Des*. 2018;132:865-880. https://doi.org/10.1016/j.cherd.2017.12.011.

33. Kaiser SC, Eibl R, Eibl D. Engineering characteristics of a single-use stirred bioreactor at bench-scale: the Mobius CellReady 3L bioreactor as a case study. *Eng Life Sci*. 2011;11(4):359-368. https://doi.org/10.1002/elsc.201000171.

34. van Eikenhorst G, Thomassen YE, van der Pol LA, Bakker WAM. Assessment of mass transfer and mixing in rigid lab-scale disposable bioreactors at low power input levels. *Biotechnol Prog*. 2014;30(6):1269-1276. https://doi.org/10.1002/btpr.1981.

35. Liepe F, Sperling R, Jembere S. *Rührwerke – Theoretische Grundlagen, Auslegung Und Bewertung*. Anhalt, Köthen: Eigenverlag FH; 1998.

36. Lee KC, Yianneskis M. A liquid crystal thermographic technique for the measurement of mixing characteristics in stirred vessels. *Chem Eng Res Des*. 1997;75(8):746-754. https://doi.org/10.1205/026387697524416.

37. Micheletti M, Nikiforaki L, Lee KC, Yianneskis M. Particle concentration and mixing characteristics of moderate-to-dense solid-liquid suspensions. *Ind Eng Chem Res*. 2003;42(24):6236-6249. https://doi.org/10.1021/ie0303799.